Characterisation of nanovoiding in dental porcelain using small angle neutron scattering and transmission electron microscopy

Alexander Lunt[1*†], Ann Terry[2], Siqi Ying[1], Nikolaos Baimpas[1‡], Tan Sui[1], Saurabh Kabra[2], Joe Kelleher[2], Stephen King[2], Neo Tee Khin[3] & Alexander M. Korsunsky[1]

1. Department of Engineering Science, University of Oxford, Parks Road, Oxford, OX1 3PJ, UK
2. ISIS Pulsed Neutron and Muon Source, Harwell Campus, Didcot, Oxfordshire, OX11 0QX, UK
3. Specialist Dental Group, Mount Elizabeth Orchard, #08-03/08-08/08-10, Singapore, 228510

† Current address: CERN, CH-1211, Geneva 23, Switzerland
‡ Current address: Atkins Ltd, London Rd, Derby DE24 8UP, UK
* Corresponding author: alexander.lunt@cern.ch, +41 22 76 63644

Abstract

Objectives: Recent studies of the yttria partially stabilised zirconia-porcelain interface have revealed the presence of near-interface porcelain nanovoiding which reduces toughness and leads to component failure. One potential explanation for these nanoscale features is thermal creep which is induced by the combination of the residual stresses at the interface and sintering temperatures applied during manufacture. The present study provides improved understanding of this important phenomenon.

Methods: Transmission electron microscopy and small angle neutron scattering were applied to a sample which was crept at 750℃ and 100 MPa (sample C), a second which was exposed to an identical heat treatment schedule in the absence of applied stress (sample H), and a reference sample in the as-machined state (sample A).

Results: The complementary insights provided by the two techniques were in good agreement and log-normal void size distributions were found in all samples. The void number density was found to be $1.61\ \mu m^{-2}$, $25.4\ \mu m^{-2}$ and $98.6\ \mu m^{-2}$ in samples A, H and C respectively. The average void diameter in sample A (27.1 nm) was found to be more than twice as large as in samples H (10.2 nm) and C (11.6 nm). The crept data showed the highest skewness parameter (2.35), indicating stress-induced growth of larger voids and void coalescence that has not been previously observed.

Significance: The improved insight presented in this study can be integrated into existing models of dental prostheses in order to optimise manufacturing routes and thereby reduce the significant detrimental impact of this nanostructural phenomenon.

Keywords

Dental porcelain, nanovoiding, small angle neutron scattering, transmission electron microscopy

Abbreviations

FIB – Focused Ion Beam

MBLEM – Multi Beam Laboratory for Engineering Microscopy

SANS – Small Angle Neutron Scattering

SEM – Scanning Electron Microscopy

TEM – Transmission Electron Microscopy

YPSZ – Yttria Partially Stabilised Zirconia

Graphical Abstract

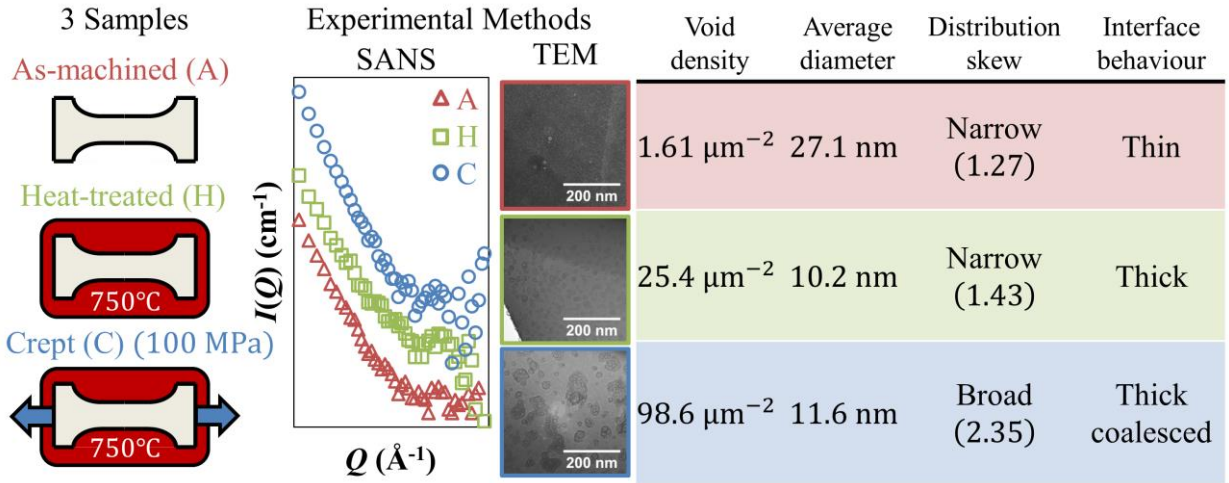

Void density	Average diameter	Distribution skew	Interface behaviour
1.61 μm^{-2}	27.1 nm	Narrow (1.27)	Thin
25.4 μm^{-2}	10.2 nm	Narrow (1.43)	Thick
98.6 μm^{-2}	11.6 nm	Broad (2.35)	Thick coalesced

1. Introduction

Recent decades have seen significant advances in ceramic processing which have facilitated the manufacture of more efficient and practical ceramic dental prostheses [1]. The appealing appearance of these systems compared to traditional metallic based implants has meant that despite questions regarding their mechanical reliability, ceramic prostheses have become popular with patients and dental technicians [2].

The exceptionally high toughness of Yttria Partially Stabilised Zirconia (YPSZ) in combination with its high strength and biocompatibility has resulted in the widespread use of this ceramic material in dental applications [3, 4]. Previously, one of the main concerns when using YPSZ in prosthesis manufacture has been the interaction between YPSZ and enamel in natural teeth [5, 6], as well as the need for managing the aesthetic appearance of the completed restoration. When used in dental prosthetics applications, YPSZ is therefore typically veneered with porcelain in order to tailor both the shade and pearlescence of the completed prosthesis and to match the appearance of natural teeth [2]. Dental porcelain is a predominantly amorphous ceramic composed of silica, alumina and a range of other oxides selected to produce a material with optimal mechanical properties and manufacturability [7, 8].

Despite the many benefits of this manufacturing approach, the origin of failure in YPSZ-porcelain prostheses is primarily located within the porcelain veneer [9]. Brittle porcelain failure may be induced at surfaces through effects such as wear faceting [10], or may nucleate at defects within the bulk material [11, 12]. Investigations into the influence of ineffective design [13, 14] and manufacturing route [15-17] have shed light onto the origins of these types of failure. For example, recent modelling and experimental studies have shown that the interaction between defects and transient stresses induced by thermal gradients increase the likelihood of failure of a porcelain veneer [11].

Fractographic studies of failed prosthesis (induced both by clinical use and simulated mastication loading) have indicated that failure can also be preferentially initiated within a few hundred microns of the YPSZ-porcelain interface [10, 18-20]. Microscale analysis has demonstrated that the microstructure and mechanical characteristics of this near-interface zone are distinct from the neighbouring regions [21, 22]. For example, one recent spatially resolved micropillar splitting study shows a significant reduction (of up to 90%) of porcelain fracture toughness within the first 100μm of the interface, as shown in Figure 1 [23]. The exact origins of this near-interface variation has so far remained unclear, although an opinion has been expressed by some researchers that failure may also be associated with the tensile residual stresses that arose

during manufacture [24-26]. Guided by these considerations, we recently used Transmission Electron Microscopy (TEM) of the YPSZ-porcelain interface region to obtain improved insight into the nanostructure of this near-interface region [21]. This analysis confirmed the presence of porcelain nanovoiding (with void sizes of ~10 nm) in a band located a few microns from the YPSZ-porcelain interface, where the residual stresses are also believed to be maximum.

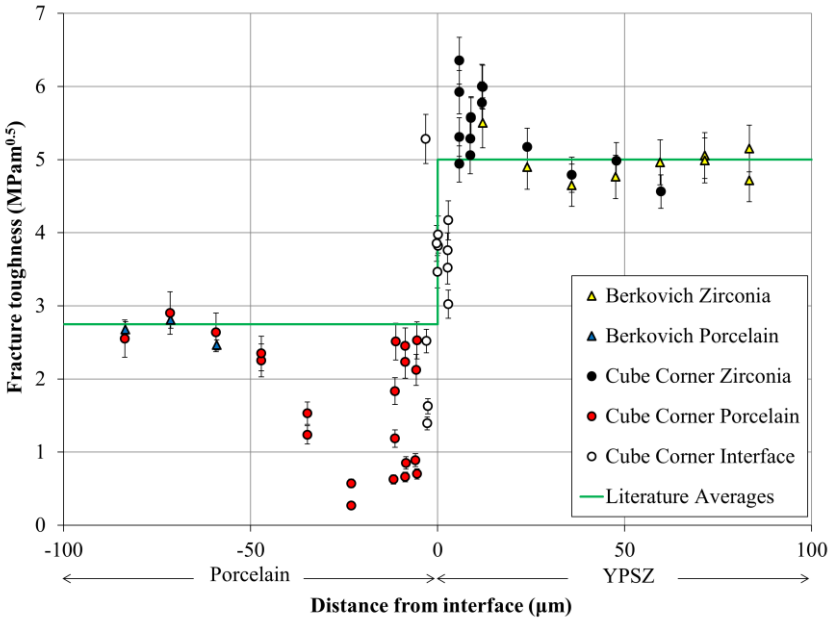

Figure 1. Results of micropillar splitting to determine the fracture toughness variation of YPSZ and porcelain within the first 100µm of YPSZ-porcelain interface. The 95% confidence intervals of each data point are shown by error bars, and an average fracture toughness for each material is shown [23].

Recent studies have also revealed that the combination of residual stress and high sintering temperatures applied to the near interface region during manufacture are sufficient to induce localised creep in dental porcelain [27]. Micro-to-nano scale void-like features have previously been observed during creep studies of porcelain and are known to lead to reduced material strength, stiffness and fracture toughness [28, 29]. The origin of this voiding behaviour is believed to be associated with the diffusional motion of vacancies within the atomic structure that induces the early onset of component failure in amorphous materials [30].

Based on the above considerations we hypothesise that porcelain creep at the YPSZ-porcelain interface leads to the generation of nanovoids that ultimately reduce the mechanical strength of this near interface region and lead to failure. Critical evaluation of this hypothesis is the subject of the present study. To assess and quantify the nanoscale porosity associated with creep, we make a comparison between three porcelain

specimens. Sample C was crept at a temperature and stress representative of the conditions present at the YPSZ-porcelain interface [16, 31], sample H was exposed to the same thermal conditions but without the application of load, and sample A represents the original as-machined state.

Only a limited number of experimental techniques can provide complete characterisation of cavitation phenomena at the nanometre length scale. In the analysis that follows two independent but complementary methods were used. Small Angle Neutron Scattering (SANS) is a reciprocal space technique based on the analysis of diffraction spectra from the samples that provides information regarding the mean shape, number density, size and distribution of voids with sizes in the range ≈1-100 nm [32, 33]. The large gauge volumes (typically >mm length scales) associated with SANS ensure that this technique provides results representative of the average bulk response, but, conversely, the technique cannot provide insight into local features [34].

To obtain spatially resolved information about nanovoiding, TEM imaging was performed on lamellae extracted from samples C, H and A. This approach benefits from direct 2D visualisation of voids, so that image post-processing can be used to assess their shape, number density, interface characteristics and distribution [34-37]. These results can be directly compared with the TEM analysis performed at the YPSZ-porcelain interface [21] and can be combined and contrasted with the results of SANS to provide improved confidence in the evaluation of nanovoiding characteristics.

2. Material and Methods

2.1. Sample Preparation

The three samples examined in this study were manufactured from a single batch of I14 Vitablocs® Mark II for Cerec [38]. Vitabloc® restorations, although composed of similar ceramics to conventional metallic or ceramic porcelain veneers, are known have a different manufacturing route, thermal characteristics and mechanical response [1]. Despite these differences, the similarities in elemental composition between these porcelain types, in combination with the carefully controlled industrial sintering process used to manufacture Vitablocs®, ensures that these components offer a comparable and microstructurally consistent base material. This high level of consistency between samples is crucial in order to identify the subtle nanoscale changes induced by the heat treatment and creep of dental porcelain.

The samples were machined using a diamond-coated grinding lathe and tensile specimen manufacturing procedure outlined by Lunt et al [27]. Multiple dog-bone samples were produced with the nominal gauge

length of 6 mm and diameter of 3.4 mm. Following a multi-stage polishing routine, the gauge diameters and lengths of each specimen were measured using a micrometer screw gauge. The reference sample in the as-machined state (sample A) was selected as one of these specimens.

High temperature creep was induced in sample C using the 50 kN uniaxial servo-hydraulic Instron loading rig at beamline Engin-X at ISIS Spallation Source, UK and the approach previously outlined by Lunt et al. [27]. The sample was placed into high temperature nickel alloy grips, a thermocouple was attached to the surface and then the sample was preloaded to around $0.2 - 0.7$ MPa in a displacement control mode. Radiant heat lamps were then used to heat the specimen up to 750 ℃ at a rate of 10 ℃min^{-1}. This holding temperature corresponds to the sintering conditions applied to dental veneering porcelains of similar composition during manufacture [39]. A thermal dwell of 3 hours was used to stabilise the system fully, ensuring that no further displacement could be observed in the loading rig output. The sample was then loaded to 100 MPa in order to match the residual stress previously observed at the YPSZ-porcelain interface of a veneer of similar thickness [22]. A loading rate of 1 MPa s^{-1} was used to minimise the likelihood of brittle failure.

The secondary creep rate behaviour of this type of dental porcelain has previously been identified elsewhere as [27]:

$$\dot{\varepsilon} = A\sigma^{n}e^{-Q/RT}, \quad (1)$$

where $\dot{\varepsilon}$ is the strain rate, A is the creep rate scaling factor ($A = 490 \pm 83.2$ MPa$^{-1.32}$s^{-1}), σ is the applied uniaxial stress, n is the stress rate exponent ($n = 1.32 \pm 0.08$) , Q is the activation energy ($Q = 243.0 \pm 3.1$ kJ mol^{-1}), R is the universal gas constant and T is the absolute temperature in K. Substitution of the sintering temperature and stress expected at the YPSZ-porcelain reveals that the corresponding strain rate is small (8.24×10^{-8}s^{-1}). Therefore, to ensure that the impact of creep on the microstructure could be clearly identified, the sample was subjected to creep loading for 96 hours to reach a nominal strain of 2.85 %. The sample was then unloaded at a rate of 1 MPa s^{-1} and cooled at a rate of 10 ℃min^{-1}.

At the end of the creep experiment, the loading rig strain reading was found to be 2.75 %. The sample was then carefully removed and a Micrometer Screw Gauge was used to measure the length of the deformed specimen which was found to correspond to a strain of 2.67 %. Despite the fact that these measurements show reasonable agreement (to their associated levels of precision), the localised necking which was observed in the gauge volume suggests that the local strain at this position may have been higher.

In order to replicate the thermal history of sample C, the remaining machined sample was placed into a Carbolite RHF 16-8 Chamber Furnace. The same ramp rate and 750 ℃ thermal dwell was applied to this heat-treated specimen (sample H).

2.2. Small Angle Neutron Scattering

SANS was performed at beamline LOQ at the ISIS Pulsed Neutron Source, UK for which a comprehensive overview of the capabilities and experimental setup has previously been published elsewhere [40]. Specially manufactured mounts were produced to hold the samples in an orientation such that their axial direction was perpendicular to the beam as shown in Figure 2. The gauge volume studied within each of the samples was aligned with the incident beam to within ~0.2mm.

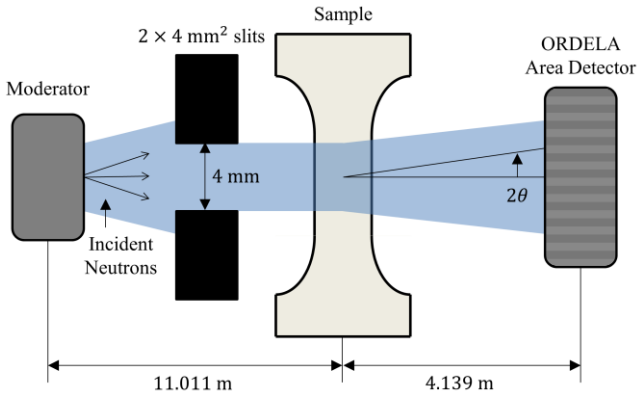

Figure 2. Schematic diagram of the SANS experiment showing moderator (source), beam defining slits, sample and detector arrangement.

Collimation of the incident beam was performed to define a 2×4 mm^2 cross sectional area. A sample to detector distance of 4.14 m, incident beam collimation length of 4.00 m and moderator to sample distance of 11.01 m were used in this study. The beam chopper was configured to define incident wavelengths between $2.2 < \lambda < 10.0$ Å at a repetition rate of 25 Hz. In order to collect sufficient statistics each sample was exposed for 6 hours corresponding to $\approx$ 0.5 mA-hours of proton flux incident on the target station. A 6 hour exposure of an empty holder was also collected in order to enable background correction.

2.3. Transmission Electron Microscopy

For TEM analysis representative lamella samples were extracted from each of the three dog-bone specimens from the location from which SANS measurements were collected. A Beuhler IsoMet® low speed diamond saw was initially used to section the sample across the gauge volume at a position just below the point where minor necking had been observed in the crept sample (C) (Figure 3). A slow cutting speed was selected to minimise the impact on the local microstructure. A multi-stage grinding and diamond grit

polishing process was next applied to the sectioned surface to remove any regions affected by sectioning. Colloidal silica polishing was finally applied to leave a smooth, uniform surface which was minimally influenced by sample sectioning.

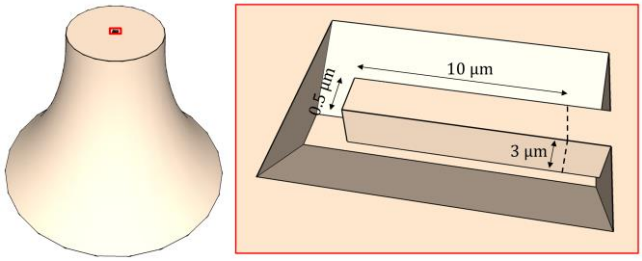

Figure 3. Schematic diagram showing sectioning location within dog-bone samples as well as the location and dimensions of the TEM lamella [41].

The three samples were mounted onto Scanning Electron Microscopy (SEM) stubs using silver paint. A 5 nm layer of Au/Pd was sputtered onto the surface of the specimens in order to improve the conduction path and thereby minimise the impact of charging during lamella preparation. The sample was then placed into the Tescan Lyra 3XM FIB-SEM at the Multi Beam Laboratory for Engineering Microscopy (MBLEM), Oxford, UK. Initial SEM imaging of the polished surfaces revealed that micro-scale voids were present in all three samples as shown in Figure 4. These voids were many orders of magnitude larger than the nano-scale voiding typically induced by creep [42] and have previously been shown to be present in as-machined samples of dental porcelain [43]. Voids of this type are believed to be associated with sintering defects induced during the manufacture of porcelain and were not the primary focus of this study, however SEM imaging of the entire cross section was performed in order to ascertain the impact of creep or heat treatment at these length scales. A working distance of 9 mm, voltage of 30 keV and pixel size of $150 \times 150\ \mathrm{nm}^2$ was used for imaging over the $\approx 9\ \mathrm{mm}^2$ cross sectional area.

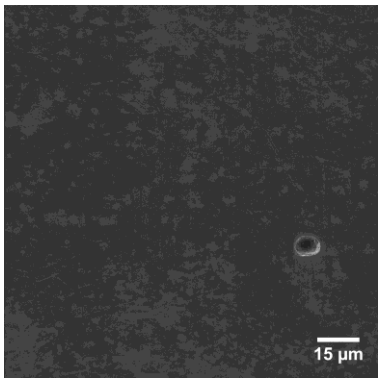

Figure 4. SEM image of cross sectional surface of sample A showing a single microscale void typical of those observed in the cross sectional surface of all three samples.

Focused Ion Beam (FIB) milling was then used to extract TEM lamella from the centre of the polished cross-sections of each sample as shown in Figure 3. The automated 'AutoSlicer' routine [41] was used to extract small sections of material with nominal dimensions of $10 \times 3 \times 0.5$ μm^3 which were attached to a copper TEM grid. Gentle FIB polishing was then performed on each of the samples using a milling current of 100 pA. The thickness of the completed lamellas was found to be $0.1 - 0.05$ μm however this process was found to reduce the visible cross sections of all samples.

TEM imaging was performed using the JEOL JEM-2100F TEM at the Research Complex at Harwell, UK. An imaging current of 1.0 μA and accelerating voltage of 200 kV was used produce a spot size of 0.25 nm during this analysis and 2056×2056 pixel images were captured at a resolution of 0.33 nm per pixel. Multiple TEM imaging was used to interrogate total areas of 22.9 μm^2, 11.6 μm^2 and 18.3 μm^2 for samples A, H and C, respectively. Example micrographs of the three samples are given in Figure 5.

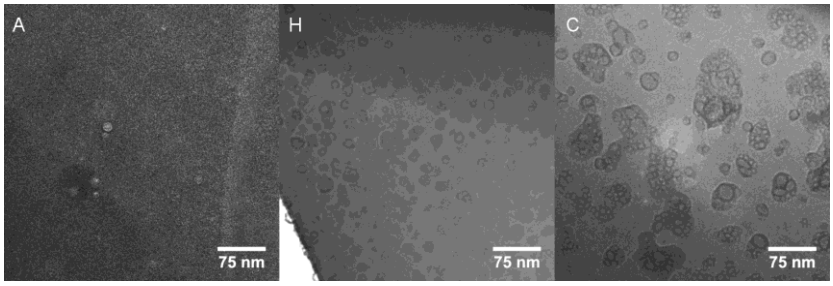

Figure 5. TEM images of the as-machined (A), heat-treated (H) and crept (C) samples.

3. Results

3.1. Neutron Scattering

In order to enable valid comparison between SANS results, care must initially be taken to determine the differences in the scattering volume between the specimens. For the three samples examined in this study the gauge volume is a 2×4 mm^2 section through the centre of a 6 mm tall cylinder which is ≈ 3.4 mm diameter. Taking into account any minor differences in diameter and the maximum offset, the expected maximum difference in gauge volume was determined to be 0.28 %. Therefore, results that show differences in the scattered intensity greater than this bound were assumed to be the consequence of the differing scattering response of the samples.

Inspection of the two dimensional SANS patterns showed no apparent anisotropy in the scattering response. Therefore the data was reduced to 1D profiles of scattered intensity versus the modulus of the scattered wavevector ($Q = \frac{4\pi}{\lambda}\sin\frac{\theta}{2}$ where λ is the incident wavelength and θ is the scattering angle as shown

in Figure 2), by radially averaging the two dimensional scattering patterns using Mantid, a neutron scattering data manipulation software package [44]. The data was then corrected for instrumental background, the measured transmission, sample volume and detector efficiency [45]. A perdeuterated/protonated polystyrene blend was used as a calibrant in order to determine measures of the absolute scattered intensity $(I(Q))$ to within $\pm$ 5 % [46] as shown in Figure 6. This procedure also gives an indirect check on the Q scale (through measurement of the polymer radius-of-gyration). In order to aid in the visualisation of the data the distributions of samples H and C have been offset by factors of 5 and 25, respectively in Figure 6.

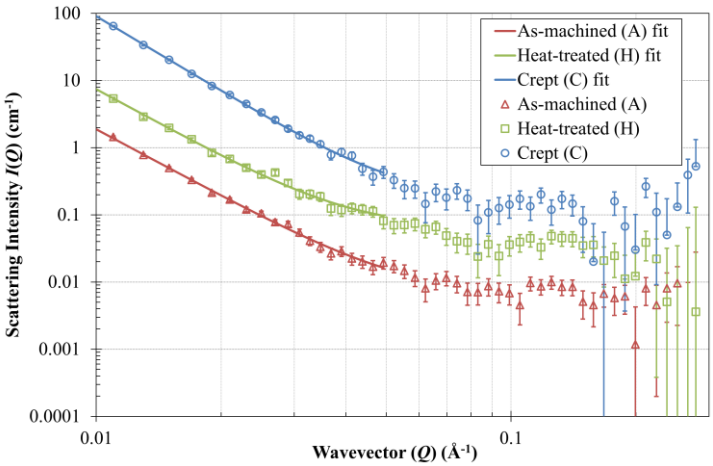

Figure 6. Intensity against wavevector for the three samples. In order to reduce the overlap between distributions samples H and C have been scaled by 5 and 25, respectively. The power law fitting is included and the error bars indicate the standard deviation of each point.

The three curves show broadly similar behaviour with a power law response at low Q (i.e. $I(Q) \sim Q^{-n}$) and fitting was performed on each of the three data sets in order to quantitatively describe the differences observed. The as-machined (A), heat-treated (H) and crept (C) samples were found to have power law exponents of 3.3, 3.2 and 3.7, respectively. Variations in the power law exponent can be indicative of differences in void shape, interface behaviour or larger (microscale) phenomena and are discussed in more detail in Section 4.3 [47].

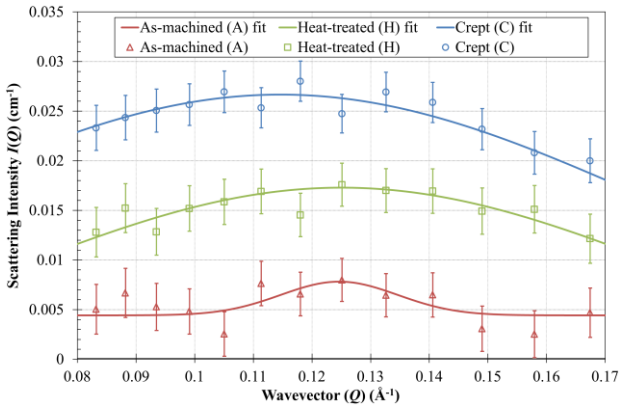

Figure 7. Intensity against wavevector in showing the peak fitting applied to the data sets. In order to reduce data overlap the heat-treated (H) and crept (C) data has been offset by 0.01 and 0.02, respectively. The error bars indicate the standard deviation of each data point.

Examination of the three scattering profiles reveals a number of peak type features overlying the power law distributions. These may be indicative of the spherical shape of the voids [48] however close inspection of the variations of intensity reveal that the confidence bounds of the associated data points are typically larger than the offsets observed. The only exception to this behaviour is observed at intermediate wavevector values ($Q = 0.08 - 0.17$ Å^{-1}) within samples H and C as shown in Figures 6 and 7.

In order to provide quantitative comparison between the three profiles at the location of interest, least squares fitting of Gaussian peak distributions was performed using the function:

$$I(Q) = f + ae^{-\frac{(Q-b)^2}{2c^2}} \tag{2}$$

where a is the peak height, b is the peak centre, c is the standard deviation and f is the background. In order to convert the peak centre estimate into the associated void dimension, the relationship between the real space $(\tilde{d})$ and reciprocal space (Q) dimensions is required:

$$\tilde{d} = \frac{2\pi}{Q}, \tag{3}$$

and the results of this analysis are given in Table 1.

Table 1. Parameter descriptors of peak centres and widths observed in the intensity vs wavevector plots. The void diameter (d) associated with each peak has also been included.

Sample	a (cm^{-1})	b (Å^{-1})	c (Å^{-1})	d (nm)
As-machined (A)	0.004	0.125	0.010	10.0
Heat-treated (H)	0.021	0.125	0.057	10.0
Crept (C)	0.027	0.111	0.063	11.3

Examination of the Gaussian fitting applied to the scattering distribution of the as-machined sample (A) reveals that the peak intensity is the same order of magnitude as the errors associated with each data point. This suggests that this peak is not statistically significant in comparison with the underlying background noise and therefore limited conclusions can be drawn from this fit.

The peak fitting analysis revealed that the average void diameter associated with the heat-treated sample (H) was smaller than in the crept sample (C) with the nominal sizes of 10.0 nm and 11.3 nm, respectively. The two peaks were also found to have different intensities, with the crept sample (C) demonstrating a peak height 28 % higher than the heat-treated sample (H). The width of the two peaks was also found to differ, with the crept sample (C) showing a broader distribution of void sizes (c values equal to 0.057 Å^{-1} and 0.063 Å^{-1} for H and C, respectively). Further details on these differences are provided in Sections 4.1 and 4.2.

3.2. Micrograph Analysis

Examination of the SEM images collected from the porcelain cross section revealed that relatively low numbers (< 50) of microscale voids were observed in all the samples. The average void diameter and standard deviations of these measurements were 4.0 ± 0.6 μm, 3.1 ± 0.5 μm, and 5.8 ± 1.3 μm for the as-machined (A), heat-treated (H) and crept (C) samples, respectively. It is interesting to note that heat treatment appears to lead to a reduction in average void size and that creep results in a moderate increase. However, the limited number of micro-voids that could be examined in this study limits any firm conclusions that can be reliably drawn on the impact of these processes on the void distribution at this length scale. The primary conclusion from this analysis is that a random distribution of voids is present prior to creep. These voids have a number density of ≈ 4.3 μm^{-2} and diameters covering the range from $1 - 20$ μm with an average of ≈ 4 μm.

In order to quantify the number and size of each of the particles within the TEM images, the 'analyse particles' subroutine within the image processing software ImageJ was used [49]. A minimum linear dimension threshold of 4 pixels (1.3 nm) was applied during processing. The outputs from this analysis include the area, perimeter, orientation and aspect ratio (maximum / minimum dimension) of each particle. The total number of particles identified was 37, 295 and 1,805 corresponding to number densities of 1.61 μm^{-2}, 25.4 μm^{-2} and 98.6 μm^{-2} for the A, H and C samples, respectively.

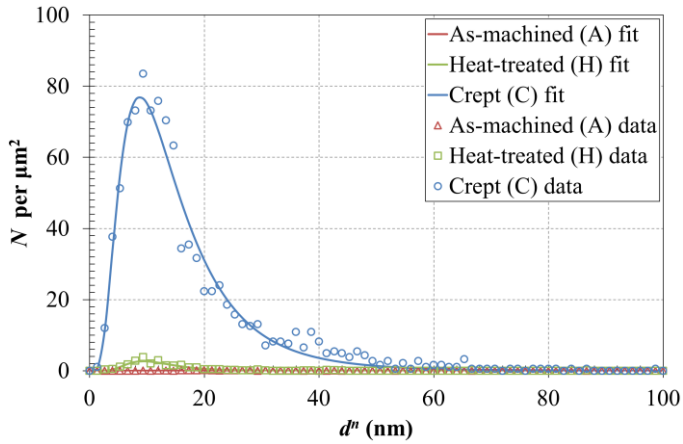

Figure 8. Histogram of void numbers per µm^2 against nominal diameter. The least squares log-normal fits of each curve are also shown.

The examination of the orientation distribution revealed that no clear preferred direction could be found in any of the samples. A broad range of particle aspect ratios were also observed in all three samples, covering the range from $1-15$. The mean value of all particles (1.77) was found to be influenced greatly by the high aspect ratio particles and therefore the median (1.366) and mode (1.094) were found to be more representative. This analysis suggests that most voids are close to spherical, with a few asymmetric outliers.

In order to obtain a representative value for the diameter of each particle the nominal diameter d^n was determined based on the cross-sectional area A:

$$d^n = 2\sqrt{\frac{A}{\pi}}. \tag{4}$$

This data was next discretised into one hundred bins 1.3 nm-wide each and normalised by dividing each data set by the cross-sectional area over which imaging was successfully performed (22.9 µm^2, 11.6 µm^2 and 18.3 µm^2 for samples A, H and C, respectively) to produce histograms of number per µm^2 against d^n as shown in Figure 8. Examination of these distributions revealed that they follow approximately log-normal variation of the form:

$$L(d^n) = \frac{\alpha\beta}{d^n\sigma\sqrt{2\pi}} e^{-\frac{\left(\ln\left(\frac{d^n}{\beta}\right)-\mu\right)^2}{2\sigma^2}}, \tag{5}$$

where μ and σ are the location and variance parameters, respectively and α and β are the vertical and horizontal scaling parameters respectively. The α scaling parameter is necessary to accommodate for the fact that these profiles are not probability density functions and therefore the area under the curve does not sum

to 1. The β scaling factor scales the data in the horizontal direction in order to account for the differences between the void mode sizes.

Least squares fitting of log-normal distribution to the three data sets was performed in order to evaluate μ, σ, α and β. These parameters can then be used to provide descriptors of the data set including the arithmetic mean $E[d^n]$ and median $\mathrm{Med}[d^n]$:

$$E[d^n] = \beta e^{\mu + \frac{\sigma^2}{2}}, \tag{6}$$

$$\mathrm{Med}[d^n] = \beta e^{\mu}. \tag{7}$$

These measures provide information on the average void diameter. To gain insight into the characteristics of the 'tail' of the distribution, the skewness of each data set can be obtained from:

$$Skew[d^n] = \left(e^{\sigma^2} + 2\right)\sqrt{e^{\sigma^2} - 1}. \tag{8}$$

Larger values of skew are indicative of the growth of voids and therefore provide quantitative descriptors of this important behaviour. The tabulated results of all statistical measures and fitted parameters are given in Table 2.

Table 2. Log-normal parameter descriptors and associated statistical measures of the void distribution histograms obtained from TEM analysis of samples A, H and C.

Sample	σ (μm)	μ (μm)	α	β	E (nm)	Med (nm)	$Skew$
As-machined (A)	0.39	0.11	0.0940	0.022	27.1	24.8	1.27
Heat-treated (H)	0.43	0.10	2.90	0.012	10.2	11.1	1.43
Crept (C)	0.61	0.10	108	0.013	11.6	12.9	2.35

For the three data sets large variations were observed between the maximum values of the void number per μm^2, N_{max} (which are shown by the highest number densities in the histogram in Figure 8). This is reflected in the relative values of α however presents difficulties when visibly comparing the distributions obtained from the three samples. In order to overcome this limitation, a normalised version of the data was replotted in which each dataset was divided by the corresponding value of N_{max} as shown in Figure 9. The peak centre and the characteristics of the distribution "tail" of the three data sets can be clearly observed.

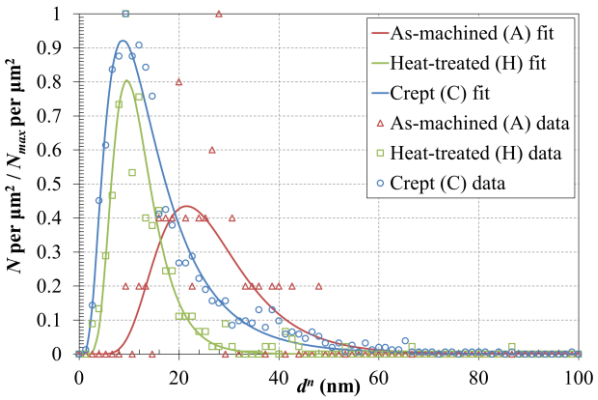

Figure 9. A histogram of void numbers per µm^2 against nominal diameter in which each data set has been normalised by N_{max}. The log-normal fits of each curve have been scaled accordingly.

4. Discussion

Examination of the body of characterisation data reveals that statistically significant differences have been detected between the as-machined (A), heat-treated (H) and crept (C) samples using both SANS and TEM analysis. It is important to reiterate at this stage that the gauge volumes of these two techniques were different, and therefore a degree of difference in the observation is to be expected. In the case of TEM analysis, the lamella was extracted from the centre of the sample at the exact location where creep-induced necking was observed. Neutron diffraction, on the other hand, was performed to provide insight into the bulk characteristics of the three samples, and therefore is a technique that delivers measurements with lower spatial resolution, but with increased statistical averaging. The presence of necking in the crept sample (C) indicates that the deformation response was induced within a subsection of the gauge volume and it is therefore perhaps unsurprising that after averaging over neighbouring regions, the changes detected in the neutron scattering data are more subtle.

4.1. Void Numbers

Examination of Figure 8 reveals that large variations in void number were detected in the TEM study. The total number of voids per unit area was found to be $1.61\ \mu m^{-2}$, $25.4\ \mu m^{-2}$ and $98.6\ \mu m^{-2}$ for samples A, H and C, respectively.

The regions of increased intensity as a function of neutron scattering wavevector correspond to the length scales for which consistent periodic variation is observed in the number of scattering features, such as interfaces or regions of high gradient of density. The average void sizes observed in the TEM analysis ($10-30$ nm diameter) correspond to equivalent Q values in the range $0.08-0.12\ Å^{-1}$. Examination of this region in the three scattering profiles reveals that the two strongest scattering peaks are observed at this

location in the heat-treated (H) and crept (C) samples. Peak fitting of these profiles has revealed that the crept data shows a 28% increase in the scattering response over that observed in the heat-treated sample (H). In the case of the as-machined sample (A), no clear peaks are observed in this region, suggesting that the void numbers are sufficiently small that they cannot be detected by SANS. This trend in the increasing scattering response matches the relative void numbers obtained by TEM analysis, indicating consistency between the techniques.

The absence of grain boundaries in amorphous materials means that creep-induced void nucleation is primarily driven by vacancy condensation [50]. The thermodynamic origins of this phenomenon have been the focus of several studies, and a number of constitutive models have been proposed to describe this response observed [51-54]. Typically these models show a negative exponential dependence upon the inverse temperature. At higher temperatures, void nucleation occurs at a faster rate. The void nucleation rate stress dependence in these models is either linear or proportional to the negative exponential of the inverse square of stress, demonstrating that larger numbers of voids are expected to initiate at higher stresses.

Although the limited number of samples examined in this study is insufficient to perform model matching or quantitative assessment of these relationships, the experimentally derived void numbers do match the relationships previously published. The largest number of voids was found in the crept sample (C) which was exposed to the highest temperature and stress combination, and the smallest number of voids was observed in the as-machined sample (A).

4.2. Void Size Distribution

The void size distributions obtained through TEM analysis are well matched by the log-normal fitting. This distribution is widely observed in particles sizes and other natural phenomena, and occurs as a result of Gibrat's law which indicates systems in which relative growth rates are independent of size [55]. This suggests that over the length scales examined in this TEM analysis, the void growth rate in porcelain is close to being uniform irrespectively of diameter. This result is perhaps surprising as below a certain threshold it is generally more energetically favourable for voids to reduce in size and ultimately annihilate [56]. However, it may simply be the case that for this system this threshold is below the TEM length scale resolution.

Examination of the mean and median void sizes obtained by TEM analysis reveals that these measures are similar for the heat-treated (H) ($E = 10.2$ nm and $\mathrm{Med} = 11.1$ nm) and crept (C) ($E = 11.6$ nm and $\mathrm{Med} = 12.9$ nm) samples. In contrast to this behaviour, the mean and median size of as-machined

sample (A) are approximately $2-3$ times larger ($E = 27.1$ and $\mathrm{Med} = 24.8$). Despite the limited number of voids observed in sample A, this significant difference indicates that the thermal processing conditions applied during manufacture were distinct from those applied during this study. In the case of the heat-treated (H) and crept (C) samples, the similarities in response indicate that the average void size is dominated by the $750℃$ hold and that a stress of 100 MPa has a limited impact on this aspect of behaviour.

In contrast to the average void size behaviour, the skewness of the as-machined (A) (1.27) and heat-treated (H) (1.43) void distributions are similar, while the skewness of the crept (C) sample is almost twice as large (2.35). This indicates that in the case of the crept sample (C), the 'tail' characteristics are more dominant than for the other two specimens. This behaviour is evident in the creep distribution shown in Figure 9 for which relatively large numbers of voids can still be seen at large values of d^n. The distinct difference in the void distribution profiles obtained through TEM analysis suggests that the application of stress drives the larger diameter void growth in porcelain.

In terms of SANS behaviour, the average size response of a particular phenomenon is indicated by the peak centre position on the intensity against wave vector plot. In the case of the as-machined (A) sample, there is a lack of clear peaks in the scattering data, and therefore no insight can be obtained into this measure. In contrast, peak fitting applied to the heat-treated (H) and crept (C) SANS results indicates the presence of voids of nominal diameters of 10.0 nm and 11.3 nm, respectively. Comparison of these diameters with the TEM analysis indicates similar behaviour in the heat-treated (H) $(10.2$ nm$)$ and crept (C) sample $(11.6$ nm$)$.

Insight into the distributions of voids within the sample can either be derived from the presence of multiple peaks or through peak broadening, with wider peaks indicating a larger variation in the nominal size of scattering medium. The standard deviation measures obtained from the Gaussian peak fitting reveals that the crept sample (C) has a broader distribution $\left(0.063\ \text{Å}^{-1}\right)$ than the heat-treated sample (H) $\left(0.057\ \text{Å}^{-1}\right)$. This is consistent with the larger values of skew observed in the TEM analysis of the crept sample (C) data.

In order to provide a more rigorous understanding of the variations in void size and distribution observed, the underlying relationships which drive this behaviour can be considered. Thermodynamic analysis of the impact of temperature on creep reveals that higher temperatures induce larger diameter voids within a broad range of ductile materials [57], as well as in the primary constituent of porcelain, silica [58]. This suggests that the large average void size in sample A is indicative of a manufacturing temperature greater than the $750℃$ applied to samples H and C. Although the exact manufacturing conditions of

Vitablocs are confidential, details have been published for similar dental porcelain ingots [59]. This method is based on melting the porcelain at temperatures above 1,000℃ (the exact temperature is not revealed) and then applying compressive pressure during cooling to reduce the build-up of pores. This high temperature process correlates well with the average pore size and low numbers of pores observed in sample A.

The wider distribution of void sizes observed in the crept sample (C) can also be explained through the underlying thermodynamics of optimal void sizes. As in the case of the heat-treated sample (H), the dominating influence on void size behaviour in the crept sample (C) is temperature. However the application of stress induces a small increase in growth rate which can be shown to act preferentially on larger pores [60, 61]. This generates a larger number of larger pores and results in a broader and more skewed void size distribution. As well as initially accommodating the increased strain energy applied to the crept sample (C), analysis has shown that broader void distributions of this type result in a more ductile material (for the same void volume fraction) which is better able to accommodate the deformation induced by creep [62].

4.3. Void Shape and Interface Behaviour

In order to gain insight into the shape and interface behaviour of the nanoscale voiding, detailed examination of the TEM images collected from each of the samples can be performed (Figure 5). In sample A this visual study reveals that within the limited number of voids in the sample, most voids are close to spherical in shape, and there is no obvious void grouping. Examination of the edge of the voids reveals a lack of distinct boundary layer suggesting that the interface of the void is sharp and contains no diffusional zone.

Although the heat-treated sample (H) contains a larger number of voids, most of them remain close to spherical in shape, and limited void clustering is observed. The main difference between this void type and that observed in sample A is the presence of a distinct boundary layer at void edges. This suggests that the interface between the void and bulk material is thicker for this sample.

Examination of the TEM image collected from the crept sample (C) reveals that although the voids are larger in number, the average void shape remains close to spherical. Similar to the heat-treated sample (H), distinct boundary layers can be observed at the edge of the void, suggesting a thicker interface than that observed in sample A. The distinguishing feature of the crept sample (C) void distribution is the void clustering behaviour that is present.

In the context of SANS, the impact of void shape and interface behaviour is indicated by the underlying distribution of intensity against wavevector. Power law fitting can be used to give a numerical descriptor of

this behaviour [63] and this approach has previously been successfully applied to study voiding behaviour in silica [64]. In this study the power law exponents for the three samples were found to be $3.3, 3.2$ and 3.7 for the as-machined (A), heat-treated (H) and crept (C) samples, respectively. These values suggest that the behaviour of the crept sample (C) is distinct from the other two specimens however care must be taken when interpreting these results, as multiple structural features are known to influence this parameter.

Variation in the average shape and connectivity of voids is known to influence the power law exponent, in the case of a dispersion of voids with limited connectivity, larger exponents indicate a more spherical void geometry [47]. However, as previously mentioned, visual examination of the TEM images reveals that the average void shape is very similar for the three samples. This conclusion is further validated by the average aspect ratios obtained from particle analysis which were found to be $1.08, 1.10$ and 1.09 for the as-machined (A), heat-treated (H) and crept (C) samples, respectively. This suggests that the differences in power exponents observed are not a consequence of void shape changes.

A second variable which is known to affect the power law exponents is the sharpness of the void-to-bulk interface, with the more gradual/diffuse transitions being associated with smaller power law exponents in the range $3 - 4$ [47]. In TEM images sharper transitions correspond to clearer interfaces between the void and the surrounding bulk material. Within the three porcelain samples it can be seen that the heat-treated (H) and crept (C) specimens have noticeably thicker diffuse interfaces and therefore that the power law exponent associated with these two samples (3.2 and 3.7) should be smaller than the as-machined (A) (3.3). This contradiction between the results of TEM and SANS analysis suggests that that there is another effect which dominates the SANS power law exponent response. One potential explanation is the microscale voiding observed using SEM analysis and this is explained in more detail in Section 4.4.

In order to consider the origins of the dark interfaces observed at the edges of the voids in the heat-treated (H) and crept (C) samples it is necessary to consider the fundamentals of TEM imaging [65]. A region containing a void has a reduced number of atoms interacting with the incident electron beam and therefore should appear lighter in a light field TEM image. In contrast to this, regions of increased disorder may interact more with the incident beam and therefore appear darker. In the case of a void surrounded by a region of increased disorder, a dark boundary layer is observed surrounding a lighter central region [66]. In some cases after travelling through the two disorder layers (top and bottom of the void), the scattering is such that the overall greyscale value is darker than neighbouring regions [67]. These regions of high disorder have

previously been observed at the void interfaces of other types of silica [42] and identical structures have previously been observed in dental porcelain at the YPSZ-porcelain interface [21].

Consideration must also be given to the void coalescence response which was observed only in the crept sample (C). Typically this clustering behaviour is considered to be energetically favourable at either a critical void growth rate or critical void volume fraction [68, 69]. As highlighted in Sections 4.1 and 4.2, the crept sample (C) has a higher volume fraction and growth rate than the other two samples, and therefore may have surpassed this threshold. The absence of clear void clustering or coalescing in dental porcelain which was exposed to similar stresses and temperatures but for a shorter time period [21] suggests that the critical parameter may be void fraction. One factor which remains unclear about the void clustering behaviour is why multiple voids are present rather than single large voids which have a lower surface energy penalty. The reason for this may simply be associated with the time taken for mass transport to remove these connections and similar arrangements have previously been observed in simulations of void coalescence [70].

4.4. Microscale effects

One of the other important considerations which needs to be taken into account when comparing relative power law exponents obtained from SANS is the influence of microscale scattering phenomena such as grain boundaries or voids [47]. Both increased numbers and larger void or grain sizes will lead to an increase in the power law exponent observed in the SANS scattering response. The lack of grains and other compositional inhomogeneous regions in this sample suggests that these two effects are unlikely to be the origin of this response. However, the microscale voiding observed through SEM imaging occurs at a length scale which may influence this behaviour.

Despite the limited numbers of voids examined in the SEM study it is interesting to note that the relative sequence of average void size determined in the analysis (4.0 μm, 3.1 μm, and 5.8 μm for samples A, H and C, respectively) is the same as in the power law fitting (3.3, 3.2 and 3.7). This suggests that the application of stress may induce a similar void growth response in both microscale and nanoscale voids. In contrast to the nanoscale response, this sequence of average void sizes would suggest that microscale voids reduce in size with the application of heat. The origins of such behaviour are not fully understood but may simply be the result of smaller voids being more energetically favourable, or preferential diffusion of larger voids towards the surface [71, 72].

5. Conclusions

In this study clear distinctions between the nanoscale voiding response of samples A, H and C have been demonstrated. The results of SANS and TEM characterisation have been shown to be generally consistent in terms of nanoscale void numbers, distribution and average size. Furthermore, the outcomes of the limited microscale void analysis are also consistent.

TEM void histograms obtained for all samples demonstrated a log-normal distribution, suggesting that the relative growth rate of nanovoids is independent of size. Similarities were also observed in the shape of the voids, with near-spherical average aspect ratios being found in all samples. The lowest void density was observed in the as-machined sample (A) ($1.61\ \mu m^{-2}$) with higher void nucleation rates resulting in increased numbers in the heat-treated (H) ($25.4\ \mu m^{-2}$) and crept (C) ($98.6\ \mu m^{-2}$) samples. The average void diameter for the heat-treated (H) (10.2 nm) and crept (C) (11.6 nm) samples were found to be similar, and to correspond to less than half of that observed in the as-machined sample (A) (27.1 nm). This suggests that the sintering temperature applied during manufacture is likely to be higher than the $750℃$ used in this study. The skewness of the three data sets was found to be $1.27, 1.43$ and 2.35 for samples A, H and C, respectively which indicates that the application of force increases the numbers of larger voids in this material. Distinct differences in the void interface behaviour were also observed, with thin edges in the as-machined sample (A), thicker boundaries in the heat-treated (H) and coalesced groups of voids identified in the crept sample (C). This suggests that a critical void fraction may have been surpassed in the case of the crept sample (C). Variations were also observed in the SANS power law exponents of the three samples ($3.3, 3.2$ and 3.7 for samples A, H and C, respectively) which corresponded closely to the ratio between average microscale void diameters determined using SEM analysis ($4.0\ \mu m, 3.1\ \mu m$, and $5.8\ \mu m$ for samples A, H and C, respectively).

These results demonstrate that a thermal dwell is sufficient to induce nanovoiding in porcelain and thereby explains the limited sintering associated with porcelain veneers of maximum mechanical strength. The application of stress during heat treatment has also been shown to increase void nucleation rates and growth rates in porcelain. This would therefore suggest that the band of nanovoiding observed at the YPSZ-porcelain interface, where high magnitude residual stresses are known to be present, is likely associated with creep in this material. Despite being exposed to an almost identical thermal history, the absence of voiding beyond this highly stressed region indicates that residual stress is necessary to induce the phenomena

observed. This region of reduced mechanical strength and toughness is known to be the primary failure location of YPSZ-porcelain dental prosthesis. Based on this insight, this study suggests that the minimisation of near interface porcelain creep through modified heat treatment and control of residual stresses is crucial to improve near-interface mechanical properties and thereby reduce the likelihood of this mode of prosthesis failure.

In order to optimise the future heat treatment routines, further study is necessary to quantify the impact of parameters such as temperature, stress and time on the generation of nanovoids in porcelain. Although examination of samples exposed to long term creep and thermal dwells has proven sufficient to easily distinguish the nanovoiding response of this material, study of samples exposed to shorter, more representative timescales is also required.

6. Acknowledgements

The European Project EU FP7 project iStress (604646) is acknowledged for the funding support provided to MBLEM, where the TEM lamella preparation milling was carried out. The authors would also like to thank the Research Complex at Harwell and the Centre for In situ Processing Studies for access to the JEM-2100F TEM. We thank STFC and ISIS for access to beamline LOQ (proposal RB1320270) that contributed to the SANS results presented here.

7. References

[1] I. Denry, J.A. Holloway. Ceramics for Dental Applications: A Review, Materials, 3 (2010) 351-368.

[2] S.A. Santander, A.P. Vargas, J.S. Escobar, F.J. Monteiro, L.F.R. Tamayo. Ceramics for Dental Restorations - an Introduction, Dyna-Colombia, 77 (2010) 26-36.

[3] I. Denry, J.R. Kelly. State of the art of zirconia for dental applications, Dent Mater, 24 (2008) 299-307.

[4] A.J.G. Lunt, M.Y. Xie, N. Baimpas, S.Y. Zhang, S. Kabra, J. Kelleher, T.K. Neo, A.M. Korsunsky. Calculations of single crystal elastic constants for yttria partially stabilised zirconia from powder diffraction data, J Appl Phys, 116 (2014) 053509.

[5] L. Wang, Y. Liu, W. Si, H. Feng, Y. Tao, Z. Ma. Friction and wear behaviors of dental ceramics against natural tooth enamel, J Eur Ceram Soc, 32 (2012) 2599-2606.

[6] W.-s. Oh, R. DeLong, K.J. Anusavice. Factors affecting enamel and ceramic wear: A literature review, The Journal of prosthetic dentistry, 87 (2002) 451-459.

[7] W.J. O'Brien. Dental materials and their selection, Quintessence Publ., 1997.

[8] C. Persson, E. Unosson, I. Ajaxon, J. Engstrand, H. Engqvist, W. Xia. Nano grain sized zirconia–silica glass ceramics for dental applications, J Eur Ceram Soc, 32 (2012) 4105-4110.

[9] I. Sailer, A. Fehér, F. Filser, L.J. Gauckler, H. Luthy, C.H.F. Hammerle. Five-year clinical results of zirconia frameworks for posterior fixed partial dentures, Int J Prosthodont, 20 (2007) 383.

[10] R. Belli, A. Petschelt, U. Lohbauer. Thermal-induced residual stresses affect the fractographic patterns of zirconia-veneer dental prostheses, Journal of the mechanical behavior of biomedical materials, 21 (2013) 167-177.
[11] P. Benetti, J.R. Kelly, A. Della Bona. Analysis of thermal distributions in veneered zirconia and metal restorations during firing, Dent Mater, 29 (2013) 1166-1172.
[12] J.B. Quinn, G.D. Quinn, V. Sundar. Fracture toughness of veneering ceramics for fused to metal (PFM) and zirconia dental restorative materials, Journal of research of the National Institute of Standards and Technology, 115 (2010) 343.
[13] M.V. Swain. Unstable cracking (chipping) of veneering porcelain on all-ceramic dental crowns and fixed partial dentures, Acta Biomater, 5 (2009) 1668-1677.
[14] A. Shirakura, H. Lee, A. Geminiani, C. Ercoli, C. Feng. The influence of veneering porcelain thickness of all-ceramic and metal ceramic crowns on failure resistance after cyclic loading, The Journal of prosthetic dentistry, 101 (2009) 119-127.
[15] P. Benetti, A. Della Bona, J.R. Kelly. Evaluation of thermal compatibility between core and veneer dental ceramics using shear bond strength test and contact angle measurement, Dent Mater, 26 (2010) 743-750.
[16] K.C. Cheung, B.W. Darvell. Sintering of dental porcelain: effect of time and temperature on appearance and porosity, Dent Mater, 18 (2002) 163-173.
[17] M. Guazzato, T.R. Walton, W. Franklin, G. Davis, C. Bohl, I. Klineberg. Influence of thickness and cooling rate on development of spontaneous cracks in porcelain/zirconia structures, Aust Dent J, 55 (2010) 306-310.
[18] M.C. Thompson, C.J. Field, M.V. Swain. The all-ceramic, inlay supported fixed partial denture. Part 2. Fixed partial denture design: a finite element analysis, Aust Dent J, 56 (2011) 302-311.
[19] B. Taskonak, J. Yan, J.J. Mecholsky Jr, A. Sertgöz, A. Koçak. Fractographic analyses of zirconia-based fixed partial dentures, Dent Mater, 24 (2008) 1077-1082.
[20] T. Sui, K. Dragnevski, T.K. Neo. Mechanisms of failure in porcelain-veneered sintered zirconia restorations. ICF13, 2013.
[21] A.J.G. Lunt, G. Mohanty, S. Ying, J. Dluhoš, T. Sui, T.K. Neo, J. Michler, A.M. Korsunsky. A Comparative Transmission Electron Microscopy, Energy Dispersive X-ray Spectroscopy and Spatially Resolved Micropillar Compression Study of the Yttria Partially Stabilised Zirconia–Porcelain Interface in Dental Prosthesis, Thin Solid Films, 596 (2015) 222-232.
[22] M. Sebastiani, F. Massimi, G. Merlati, E. Bemporad. Residual micro-stress distributions in heat-pressed ceramic on zirconia and porcelain-fused to metal systems: Analysis by FIB–DIC ring-core method and correlation with fracture toughness, Dent Mater, (2015).
[23] A.J.G. Lunt, G. Mohanty, T.K. Neo, J. Michler, A.M. Korsunsky. Microscale resolution fracture toughness profiling at the zirconia-porcelain interface in dental prostheses, SPIE Micro+ Nano, (2015) 96685S-96685S-96611.
[24] Y. Zhang, M. Allahkarami, J. Hanan. Measuring residual stress in ceramic zirconia–porcelain dental crowns by nanoindentation, J Mech Behav Biomed Mater, 6 (2012) 120-127.
[25] M.P. Dittmer, L. Borchers, M. Stiesch, P. Kohorst. Stresses and distortions within zirconia-fixed dental prostheses due to the veneering process, Acta Biomater, 5 (2009) 3231-3239.
[26] H. Haskan, T. Boyraz, M.A. Kilicarslan. Investigation of thermal stresses in dental restoration by mathematical method, J Eur Ceram Soc, 27 (2007) 899-902.
[27] A.J.G. Lunt, S. Kabra, J. Kelleher, S.Y. Zhang, T.K. Neo, A.M. Korsunsky. Tensile Secondary Creep Rate Analysis of a Dental Veneering Porcelain, Thin Solid Films, 596 (2015) 269-276.
[28] R. Ponraj, S.R. Iyer, V.M. Radhakrishnan. Creep of porcelain-containing silica and alumina, J Mater Sci, 29 (1994) 4385-4392.
[29] A.A. Wereszczak, K. Breder, M.K. Ferber, T.P. Kirkland, E.A. Payzant, C.J. Rawn, E. Krug, C.L. Larocco, R.A. Pietras, M. Karakus. Dimensional changes and creep of silica core ceramics used in investment casting of superalloys, J Mater Sci, 37 (2002) 4235-4245.

[30] Y.S. Na, J.H. Lee. Interpretation of viscous deformation of bulk metallic glasses based on the Nabarro–Herring creep model, J Mater Process Tech, 187–188 (2007) 786-790.
[31] A.J.G. Lunt, T.K. Neo, A.M. Korsunsky. An Electron Microscopy Study of Sintering in Three Dental Porcelains, Proc WCE, 2 (2015).
[32] R. Lapovok, D. Tomus, J. Mang, Y. Estrin, T.C. Lowe. Evolution of nanoscale porosity during equal-channel angular pressing of titanium, Acta Mater, 57 (2009) 2909-2918.
[33] Y.B. Melnichenko, G.D. Wignall. Small-angle neutron scattering in materials science: Recent practical applications, Journal of Applied Physics, 102 (2007) 021101.
[34] C. Heintze, F. Bergner, A. Ulbricht, H. Eckerlebe. The microstructure of neutron-irradiated Fe–Cr alloys: A small-angle neutron scattering study, J Nucl Mater, 409 (2011) 106-111.
[35] J. Li, Z.L. Wang, T. Hufnagel. Characterization of nanometer-scale defects in metallic glasses by quantitative high-resolution transmission electron microscopy, Physical Review B, 65 (2002) 144201.
[36] H.-J. Kleebe, W. Braue, H. Schmidt, G. Pezzotti, G. Ziegler. Transmission electron microscopy of microstructures in ceramic materials, J Eur Ceram Soc, 16 (1996) 339-351.
[37] R. Nakamura, M. Ishimaru, A. Hirata, K. Sato, M. Tane, H. Kimizuka, T. Shudo, T.J. Konno, H. Nakajima. Enhancement of nanovoid formation in annealed amorphous Al2O3 including W, Journal of Applied Physics, 110 (2011) 064324.
[38] Vitablocs for Cerec / inLab Working Instructions.https://www.vita-zahnfabrik.com/en/VITABLOCS-Mark-II-25030,27568.html. 10/03/2015.
[39] IPS e.max Ceram.http://www.ivoclarvivadent.co.uk/en/products/all-ceramics/ips-emax-technicians/ips-emax-ceram. 19/02/15.
[40] R. Heenan, J. Penfold, S. King. SANS at pulsed neutron sources: present and future prospects, J Appl Crystallogr, 30 (1997) 1140-1147.
[41] AutoSlicer - Sample Preparation Tool.http://www.tescan.com/en/other-products/software/autoslicer-sample-preparation-tool. 19/02/15.
[42] F. Lofaj, A. Okada, H. Usami, H. Kawamoto. Creep Damage in an Advanced Self-Reinforced Silicon Nitride: Part I, Cavitation in the Amorphous Boundary Phase, J Am Ceram Soc, 82 (1999) 1009-1019.
[43] K. Anusavice, B. Hojjatie. Tensile stress in glass-ceramic crowns: effect of flaws and cement voids, Int J Prost, 5 (1991) 351-358.
[44] O. Arnold, J.-C. Bilheux, J. Borreguero, A. Buts, S.I. Campbell, L. Chapon, M. Doucet, N. Draper, R.F. Leal, M. Gigg. Mantid—Data analysis and visualization package for neutron scattering and μ SR experiments, Nucl Instrum Meth A, 764 (2014) 156-166.
[45] R. Heenan, S. King. Development of small-angle diffractometer LQD at the ISIS pulsed neutron source, Proc Int Sem Struct, (1993).
[46] B. Hammouda, R.M. Briber, B.J. Bauer. Small angle neutron scattering from deuterated polystyrene/poly (vinylmethyl ether)/protonated polystyrene ternary polymer blends, Polymer, 33 (1992) 1785-1787.
[47] J.M. Carpenter, C.K. Loong. Elements of Slow-Neutron Scattering: Basics, Techniques, and Applications, Cambridge University Press, 2015.
[48] L.A. Feigin, D.I. Svergun. Structure Analysis by Small-Angle X-Ray and Neutron Scattering, Springer US, 2013.
[49] M.D. Abràmoff, P.J. Magalhães, S.J. Ram. Image processing with ImageJ, Biophoton Int, 11 (2004) 36-43.
[50] K. Weinberg. Void nucleation by vacancy condensation, PAMM, 8 (2008) 10249-10250.
[51] J.W. Christian. The theory of transformations in metals and alloys, Newnes, 2002.
[52] R. Raj, M.F. Ashby. Intergranular fracture at elevated temperature, Acta Metall Mater, 23 (1975) 653-666.
[53] J.P. Hirth, W.D. Nix. Analysis of cavity nucleation in solids subjected to external and internal stresses, Acta Metall Mater, 33 (1985) 359-368.
[54] R.L. De Orio, H. Ceric, S. Selberherr. Physically based models of electromigration: From Black's equation to modern TCAD models, Microelect Rel, 50 (2010) 775-789.

[55] H.D. Rozenfeld, D. Rybski, J.S. Andrade, M. Batty, H.E. Stanley, H.A. Makse. Laws of population growth, Proce Nat Aca Sci, 105 (2008) 18702-18707.
[56] F.D. Fischer, J. Svoboda. Void growth due to vacancy supersaturation – A non-equilibrium thermodynamics study, Scripta Mater, 58 (2008) 93-95.
[57] M. Horstemeyer, S. Ramaswamy. On factors affecting localization and void growth in ductile metals: a parametric study, Inter J Dam Mech, 9 (2000) 5-28.
[58] M. Liehr, J. Lewis, G.W. Rubloff. Kinetics of high-temperature thermal decomposition of SiO2 on Si (100), J Vac Sci Tech A, 5 (1987) 1559-1562.
[59] IPS e.max® Ceram Scientific Documentation www.roedentallab.com/downloads/emaxceramicdata.pdf. 19/02/15.
[60] E. Seppälä, J. Belak, R. Rudd. Effect of stress-triaxiality on void growth in dynamic fracture of metals: a molecular dynamics study, arXiv preprint cond-mat/0310541, (2003).
[61] B. Liu, X. Qiu, Y. Huang, K.C. Hwang, M. Li, C. Liu. The size effect on void growth in ductile materials, Journal of the Mechanics and Physics of Solids, 51 (2003) 1171-1187.
[62] A. Melander, U. Ståhlberg. The effect of void size and distribution on ductile fracture, Int J Fract, 16 (1980) 431-440.
[63] G. Beaucage. Approximations leading to a unified exponential/power-law approach to small-angle scattering, J Appl Crystallogr, 28 (1995) 717-728.
[64] S. Sinha, T. Freltoft, J. Kjems. Observation of power-law correlations in silica-particle aggregates by small angle neutron scattering, Kinet Aggreg Gela, 19842 (1984) 87-90.
[65] D.B. Williams, C.B. Carter. The transmission electron microscope, Springer, 1996.
[66] A. Mahapatra, U. Bhatta, T. Som. Oxidation mechanism in metal nanoclusters: Zn nanoclusters to ZnO hollow nanoclusters, J Phys D, 45 (2012) 415303.
[67] G. Krishnan, B.J. Kooi, G. Palasantzas, Y. Pivak, B. Dam. Thermal stability of gas phase magnesium nanoparticles, J Appl Phys, 107 (2010) 053504.
[68] T. Pardoen, I. Doghri, F. Delannay. Experimental and numerical comparison of void growth models and void coalescence criteria for the prediction of ductile fracture in copper bars, Acta Mater, 46 (1998) 541-552.
[69] Y. Gao. Improvement of fatigue property in 7050–T7451 aluminum alloy by laser peening and shot peening, Mat Sci Eng A, 528 (2011) 3823-3828.
[70] E. Seppälä, J. Belak, R. Rudd. Onset of void coalescence during dynamic fracture of ductile metals, Phys Rev Lett, 93 (2004) 245503.
[71] Y. Takahashi, F. Ueno, K. Nishiguchi. A numerical analysis of the void-shrinkage process controlled by surface-diffusion, Acta Metall Mater, 36 (1988) 3007-3018.
[72] Y. Takahashi, K. Inoue, K. Nishiguchi. Identification of void shrinkage mechanisms, Acta Metallurgica et Materialia, 41 (1993) 3077-3084.